

Structural Health Monitoring of a Steel Railway Bridge using Optical Fibre Bragg Grating Sensors and Numerical Simulation.

George J. Tsamasphyros, Elias A. Koulalis, George N. Kanderakis, Nikos K. Furnarakis, Vangelis Z. Astreinidis

National Technical University of Athens, Department of Engineering Science, Section of Mechanics, Athens, Greece – gkandera@central.ntua.gr

ABSTRACT

The application of structural health monitoring techniques to a late 19th century steel railway bridge located at Nea Peramos near Athens Greece, still under regular usage, has been attempted using optical fiber Bragg grating sensors. As a first step, one fiber Bragg grating sensor was placed in the middle of a secondary beam section, exactly below the rail track on the one edge of the bridge and measurements have been retrieved for trains entering the bridge from both edges, crossing at a speed of approximately 60km/hr. The experimental results were compared against finite element model of the bridge, which took into account the variation of the loads versus time. Despite the existence of a number of modeling error factors (static finite element analysis, weight approximation, local plasticity of the bridge material due to aging etc.) the experimental results were found to be in very good qualitative and quantitative accordance with the numerical ones. Further work is planned to be performed using additional optical sensors as well different types of sensors, while the effects of typical structural damages (cracks, bolt damage etc.) will be experimentally investigated and numerically simulated.

Key words: Structural Health Monitoring, Optical Fibers, Bridge monitoring

1. Introduction

Structural health monitoring is a relatively new scientific field which aims in providing reliable data concerning the integrity of different kind of structures, in order to permit their further operational utilization or to impose their repair or retirement. For this reason, a variety of cheap, accurate and reliable sensors are placed over the critical points of a structure (e.g. stress concentration areas) which provide data during the normal operation of the structure. Comparing these data versus the standard structural behavior (as retrieved through analysis and/or previous experimental measurements) real time monitoring of the structural integrity is enabled and areas of flaws can be identified. Using this novel technique, numerous uncertainties which are presented during the initial structural design phase (precise loading conditions, exact structural behavior etc.) can be efficiently treated, leading to the application of lower safety factors. Moreover, early diagnosis of potential manufacturing flaws is enabled, minimizing the risk of damages and accidents during normal operation of the structure, due to their fatigue propagation. It should be underlined that such benefits are provided without necessitating the temporary retirement of the structure from its operational usage (which is the case when applying conventional Non Destructive Inspection methods) and with relatively low cost (which is constantly decreasing following the trend of all kind of electronic equipment). It is well understood that, in case a deviation versus normal behavior which exceeds certain limits is detected, a thorough investigation (usually involving standard NDI methods) has to be carried out, in order to identify the exact flaw location, type and

magnitude and to specify the appropriate repair method or to decide the retirement of the structure from operation.

The main steps in order to implement the structural health monitoring methodology are the following:

- *Selection of appropriate locations for installation of sensor:* This is performed through detailed simulation of the expected structural behavior, in order to identify any potentially critical locations (e.g. stress concentration areas or maximum deformation regions). Moreover, the appropriate type of sensors has to be selected, according to the type of measurement to be performed, the required accuracy and the operational environment.
- *Structural data collection:* This usually takes place under both normal operational and maximum loading conditions, by retrieving the maximum number of measurements possible. Accurate knowledge of the loading conditions is required, in order to make reliable comparisons versus standard behaviour.
- *Comparison of retrieved measurements versus standard behavior.* This is the last and most difficult phase, which involves the evaluation of all collected data, in order to decide whether a structural failure exists and to precise (as much as possible) its nature, position and magnitude.

Detailed description of the structural health monitoring methodology can be found in [1-9]. Within this paper, the above mentioned steps have been implemented in order to verify their applicability over a steel railway bridge subject to variable loading conditions (train crossing), using optical FBG sensors. A late 19th century steel railway bridge located at Nea Peramos near Athens Greece, which is still under regular usage, has been selected and, as a first step, one fiber Bragg grating sensor has been installed, in order to retrieve strain measurements during train crossings. The experimental data collected have been compared against the finite element model, which was created using commercial FE software.

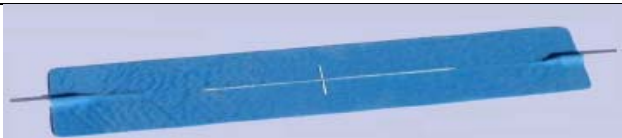
2. Hardware

2.1 Optical fibre sensors

For the performance of this study Commercial Of The Shelf (COTS) optical fiber Bragg Gratings sensors embedded into thin composite patches (Smart Patch[®]), produced by the Smart Fibers Ltd, have been used. The Bragg Grating sensor operates in the 1520-1570 nm area and is sensitive to both mechanical and temperature field variations. The induced wavelength variation is calculated through the formula:

$$\Delta\lambda = K_\epsilon \epsilon_z + K_T \Delta T \quad (1)$$

Table 1: Basic Smart Patch[®] technical characteristics.


Resolution	0.2 pm	Wavelength
	0.2 μ strain	Strain
	0.02 °C	Temperature
Optical cable	3mm Diameter - PVC protection using Kevlar fibers	
Optical fiber type	Single mode 9/125 μ m -250 μ m Acrylate coat	
Sensor type	Wavelength: 1520-1570nm - R>90%	
Sensor length	0.1 – 10mm	
Strain range	\pm 20.000 μ strain	
Optical connector	FC/APC	
Power supply	-	
Operating temperature	-100 to 300 °C	

As provided by the manufacturer, the value of K_{ϵ} , which correlates strain to wavelength, is 1.2 pm/ μ strain, while K_T , correlating thermal to wavelength variations, is 11 pm/ $^{\circ}$ C. Table 1 summarizes the basic technical characteristics of the Smart Patch[®], while more detailed information about their operation could be found in [10,11,12].

2.2 Optical Interrogator

A COTS optical interrogator procured through Micron Optics has been used for data collection, capable of applying a 100Hz sampling frequency (i.e. 100 measurements per minute per sensor). This interrogator enables extended multiplexing (up to 128 sensors per channel, 2 channels maximum), while providing network connection capability through its Ethernet port, in order to facilitate the performance of remote, real time measurements. Table 2 summarizes the basic technical characteristics of the optical interrogator which was used, while additional information can be found in [10,11,13].

Table 2: Basic technical characteristics of the optical interrogator which was used.

Resolution	0.2 pm	<i>Wavelength</i>
	0.2 μ strain	<i>Strain</i>
	0.02 $^{\circ}$ C	<i>Temperature</i>
Repeatability	\pm 1 pm	<i>Wavelength</i>
	\pm 0.8 μ strain	<i>Strain</i>
	0.09 $^{\circ}$ C	<i>Temperature</i>
Wavelength range	1520-1570 nm	
Number of channels	2	
Maximum number of sensors per channel	128	
Max. sampling frequency	100 Hz	
Interface	Ethernet	
Optical connector	FC/APC	
Power supply	24VDC/220VAC	
Operating temperature	10 – 40 $^{\circ}$ C	

2.3 Sensor placement

The Smart Patch[®] sensor bonding process is similar to the one followed for adhesively bonded composite repair of steel structures (composite patch repair). The adhesive used was the SP106 epoxy resin system, manufactured by the SP Systems company [14]. It should be noted that the bonding procedure which is applied is practically common for both metallic and concrete structures, involving:

- Marking of the sensor's position.
- Cleaning with soft detergent from any grease remains.
- Mechanical abrasion of the bonding area.
- Cleaning of debris using compressed air or brush.
- Thorough cleaning of the bonding area using acetone or equivalent cleaning agent.
- Full open air drying of the bonding area.
- Initial adhesive preparation, through mixing of ingredients (resin – catalyst).
- Application of a thin adhesive layer over the bonding area and the Smart Patch[®] sensor.
- Placement of the Smart Patch[®] sensor over the bonding area.
- Pressure application over the sensor (approximately 8-10Kg) until the end of the adhesive curing. *Extreme caution should be taken in order to prohibit any sensor sliding over the bonding area.*

3 Steel railway bridge

3.1 General description

The steel railway bridge located at Nea Peramos near Athens Greece (Figure 1) was constructed during the late 19th century and has undergone several repairs / reinforcements since then, last one taking place at 1968. The material used for its construction was mild steel, for increased strength and ductility.



Figure 1 : Nea Peramos steel railway bridge

3.2 Structural description

The steel structure of the bridge is composed of two main external beams 10.90m long, which is the total bridge length, the width being 3.70m. The wooden supports, over which the rail tracks are fixed, are based on two secondary beams (distance between them 1.40m), which are supported on the main ones through 5 lateral beams, 3.60m long, repeated every 2.725m. Steel bolts are used for all the connections between the beams, while the connection areas are reinforced by doublers. Given that the bridge is situated on a curve ($R=200m$), the external track is 0.121m higher than the internal one. All the beams used have an I-type cross section, while certain areas have been reinforced using additional L-type beams. All the cross sections used for the construction of the bridge are presented in Figure 2. The metallic structure is leaning on two reinforced concrete supports, in a way that adequate space for thermal expansion effects is left. The 0.20 x 0.20 x 2.00m rail tracks wooden supports lean over the secondary beams every 0.30m, their weight being $8KN/m^3$. The weight of the rail tracks is 60Kg/m.

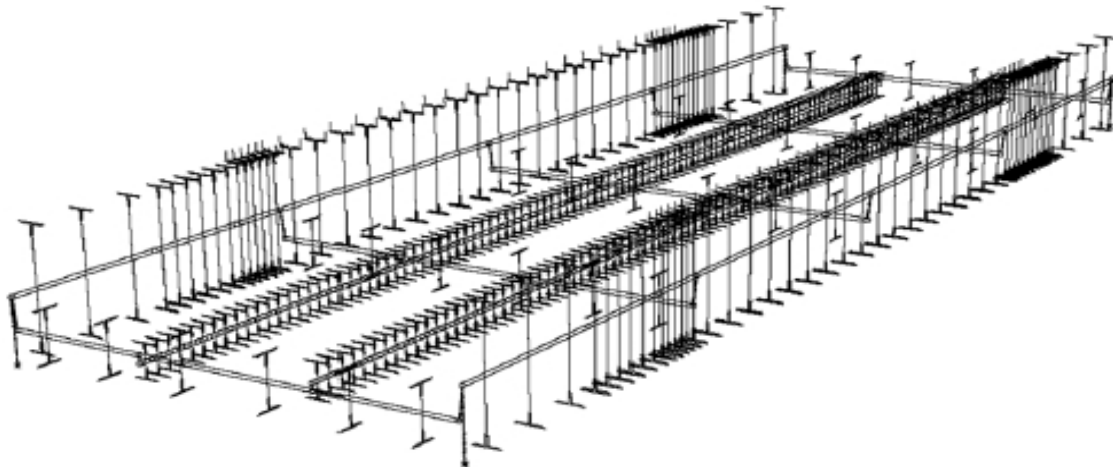


Figure 2: Cross sections of beams used for the construction of the bridge.

3.3 Sensor bonding position.

The position for the sensor bonding was selected according to the results of the finite element analysis model. The sensor was bonded exactly half way under the first part of the secondary beam, 1.36m away from the bridge support area, as shown in Figure 3, thus enabling the direct secondary beam strain measurement during the train crossing.

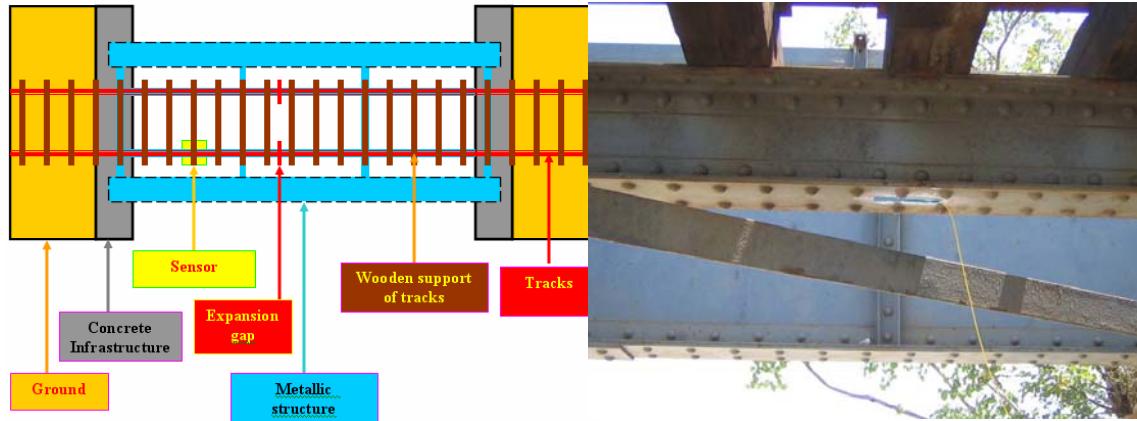


Figure 3: Sensor's position

4. Experimental results

Using the W3/2100 optical interrogator, connected to a laptop for data collection, the reflected wavelength (λ) over time (t) during train crossing was recorded. Given that the train crossing duration (and consequently the wavelength recording period) was approximately 5-6 sec, the temperature variation effects to the recorded wavelength were considered negligible. Consequently, the wavelength variations ($\Delta\lambda$) recorded were the result of mechanical loading only, which means that equation (1) is reduced to:

$$\Delta\lambda = K_e \varepsilon_z \quad (2)$$

The experimental measurements were retrieved during the crossing of 3-carriage trains, with a total length of 59.10m and width of 2.70m. Their maximum gross weight (including passengers, fuel etc.) is 153tn, while every carriage is supported by two double axis on each end, as shown in Figure 4. The train crossing speed was approximately 60km/hr.

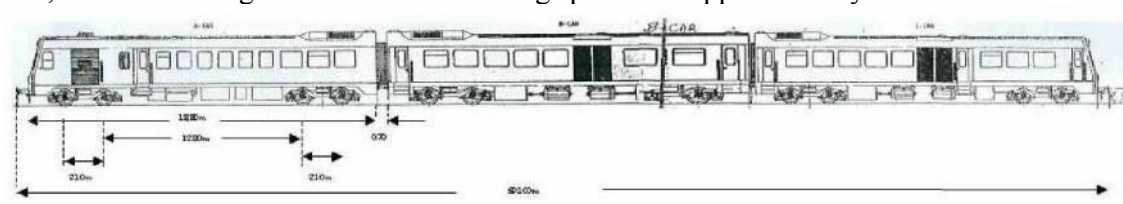


Figure 4: Side view and basic dimensions of the train crossing the bridge during data collection.

An indicative strain (μ strain) versus time (1/100 sec) curve, as computed using the wavelength data collected during the train crossing, is presented in Figure 5.

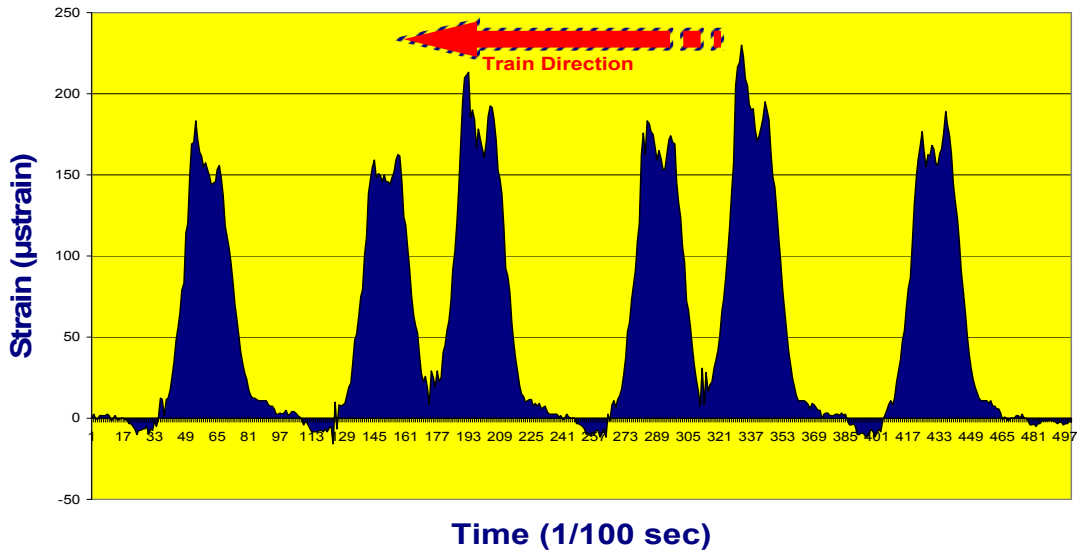


Figure 5: Indicative strain versus time diagram, during train crossing.

The 12 (2x6) strain peaks shown in the diagram correspond to the 12 train axis crossing over the sensor position, given that at this point of time the secondary beam presents maximum deformation. Compression loading is initially monitored before those peaks, which is the result of inverse bending, caused by the train entering the bridge from the other end, compared to the sensor's position. Finally, periodic abrupt variations of strain is noticed just before the normal increase of strain, which is due to the crossing of wheels over the expansion gaps, which are located over the transverse beams, in order to minimize the vibrations and strains generated during train crossing. Figure 6 presents a qualitative explanation of the experimental results, corresponding to the consecutive crossing of 4 axis (2 aft axes of the 1st carriage and 2 forward axis of the 2nd carriage), of 1.3 sec total duration.

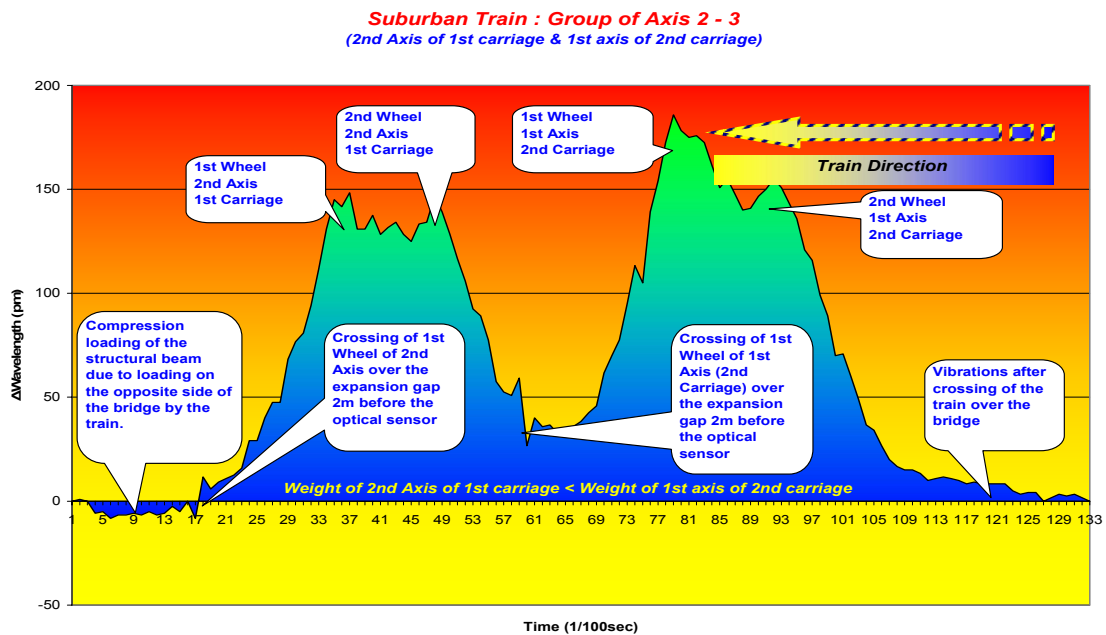


Figure 6: Qualitative explanation of the experimental results (consecutive crossing of 4 axis : 2 aft axes of the 1st carriage and 2 forward axis of the 2nd carriage).

4. Numerical Simulation

4.1 General

In order to select the optimum sensor position and to enable the evaluation of the experimental results, detailed numerical simulation was performed, using the SOFiSTiK finite element analysis program. Fe360(S235) steel ($E=210\text{GPa}$, Poisson ratio $\nu=0.30$) was chosen as the construction material, assuming linear elastic behavior. Moreover, it was assumed that all structural deformations are small and the structure is behaving in a linear elastic way.

4.2 Geometry of the structure – Meshing

The geometrical characteristics of the bridge were input according to the architectural drawings, by means of nodes which were interconnected using beam elements. Every beam element was linked against the six (6) different beam cross sections, which are used in the bridge, while the moment of inertia and the center of gravity of each beam section were calculated by the finite element analysis program. Due to the fact that the connection between the beams does not always coincide to their centers of gravity, additional auxiliary nodes were defined, in order to achieve representative interconnections. The beam's connections were simulated by means of node couplings, while the program calculated automatically the appropriate stiffness zones. The bridge meshing was performed initially automatically and finer meshing was created at stress concentration areas. Finally, additional nodes were created along the secondary beams (every 109mm) in order to better simulate the applied loading conditions (consecutive moving of the train)

4.3 Loading conditions

The applied loads on the bridge are of two types: permanent and moving. The permanent loads include the weight of the metallic structure, as well as the weights of the rail tracks and their wooden supports. The weight of the steel structure was calculated automatically by the programme, according to the dimensions of the structural elements, while the additional loads were input on the secondary beams in terms of kN/m. The moving loads were input using appropriate macros, simulating the first 6 train axis passing over the sensor. The applied load per axis was 127.5 kN, equally shared between the two wheels.

4.4 Numerical results

According to the computed displacements and rotations at each time step over the edges of the element where the sensor was bonded, induced strains were calculated applying the theory of beam subject to bending [15]: a beam (e) of length s , constant cross section A and Young modulus E is considered. The beam is located on a local coordinate system starting at i , while the coordinate system axis x coincides with the beam ij , with direction from i to j . Axis y,z coincide with the principal beam axis. The beam edges are subject to moments My_i, My_j , as shown in Figure 7.

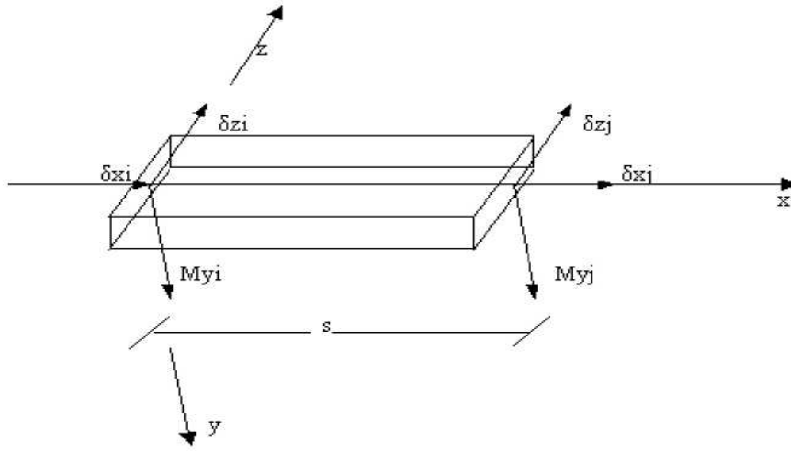


Figure 7 : Beam subject to bending.

In such case, the strains are calculated according to the following formula:

$$\varepsilon = \frac{1}{s^2} \begin{pmatrix} -s & 0 & 0 & s & 0 & 0 \\ 0 & -6(2\xi - 1)z & -2s(3\xi - 2)z & 0 & -6(1 - 2\xi)z & -2s(3\xi - 1)z \end{pmatrix} \begin{Bmatrix} \delta_{xi} \\ \delta_{zi} \\ \theta_{yi} \\ \delta_{xj} \\ \delta_{zj} \\ \theta_{yj} \end{Bmatrix} \quad (3)$$

where $\xi = \chi/s$
 χ = distance
 s = total beam length

The induced strain for each time step is calculated by the difference between the strain in “unloaded” condition (i.e. application of the permanent loads only) and the strain in loaded condition (during the train crossing). Given that the sensor was bonded under the middle of the beam section, $\xi=1/2$ was selected, while z was set to $z=-144.5$ mm, because the strain value at the lower flange of the beam was required (289 mm is the total beam height). It should be noted that as beam length (s), the sum of the initial beam length (109 mm) in addition to the beam extension due to the application of the permanent loads was considered (total $s=109.0282$ mm). The numerically calculated strain diagram versus load steps is shown in Figure 8.

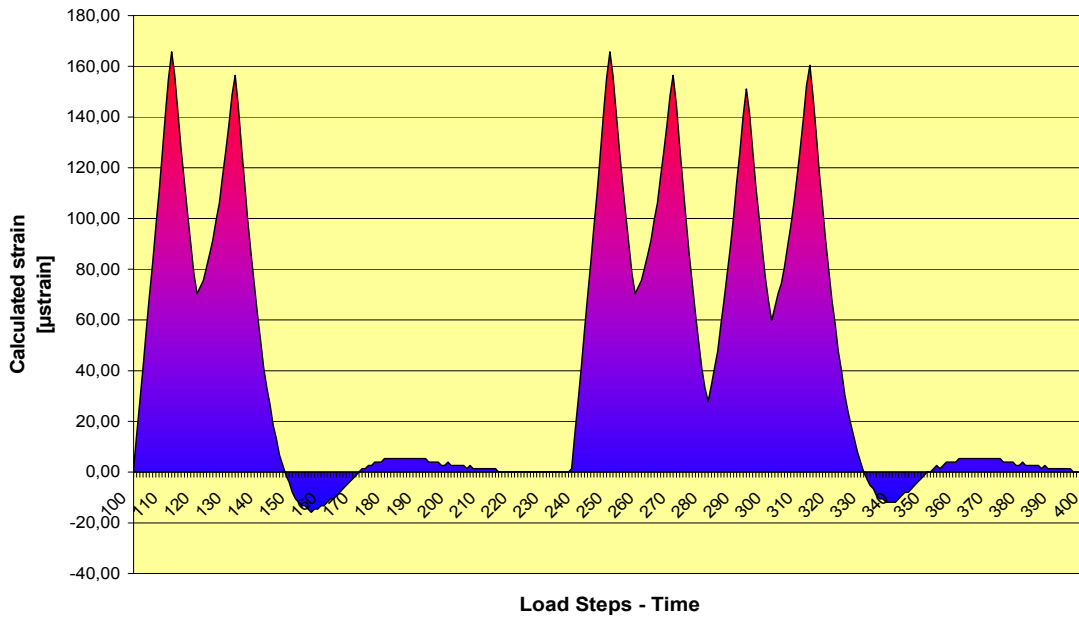


Figure 8: Numerically calculated strain diagram versus load steps

5. Comparison of experimental versus experimental results

In order to achieve a better comparison of results, the numerical calculations were merged with the equivalent experimental measurements in common diagrams (Figures 9-10), by matching the load steps of the numerical model to the corresponding load application time, as recorded in the experimental results. The numerical results presented in these Figures correspond to trains full by 2/3 with passengers and concern trains entering the bridge from both the sensor's side and the opposite of the sensor's side.

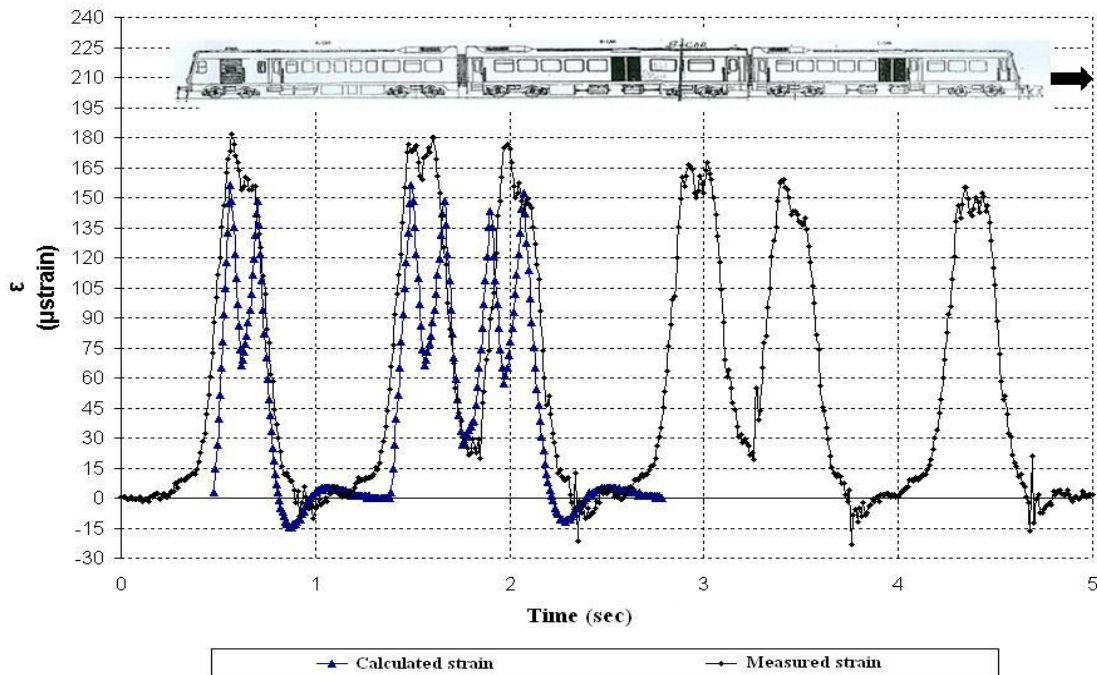


Figure 9: Comparison of experimental measurements versus numerical calculations during train crossing (train entering the bridge from sensor's side).

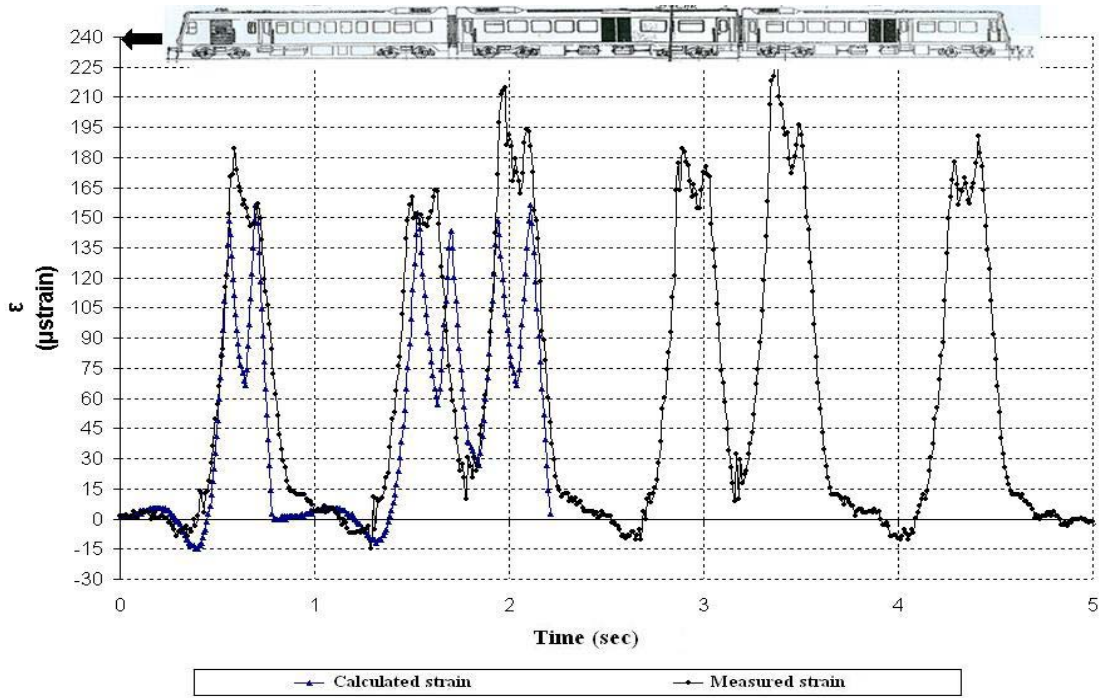


Figure 10: Comparison of experimental measurements versus numerical calculations during train crossing (train entering the bridge from the opposite of the sensor's side).

Moreover, in Table 3 the maximum calculated strain values are recorded and their difference compared to the experimental measurements is presented.

Table 3: Maximum calculated strain values compared to the experimental measurements.

		Axis Number	1	2	3	4	5	6
<i>Experimental Results</i>	Train 1	Strain (μstrain)	184.5	157.0	160.4	162.9	214.5	192.9
			190.4	177.9	184.5	175.4	231.2	196.2
	Train 2	Strain (μstrain)	181.6	155.8	176.6	180.0	176.7	146.7
			150.8	145.8	165.8	167.5	159.2	140.0
	Average	Strain (μstrain)	176.9	159.2	171.9	171.5	195.4	168.9
<i>Numerical Results</i>	Train Load = 2/3 Maximum	Strain (μstrain)	156.4	148.4	156.4	148.4	143.1	152.4
		Difference (%)	13.1	7.2	9.9	15.5	36.5	10.9
	Train Load = 3/3 Maximum	Strain (μstrain)	165.7	156.4	165.7	156.4	151.1	160.4
		Difference (%)	6.7	1.7	3.7	9.6	29.3	5.3

According to the comparison between the numerical results and the experimental measurements, it is concluded that very good qualitative and quantitative consistency was achieved:

- The maximum strain values are generally within a limit of 15% difference compared to the experimental results. However, it should be noted that the recorder strain values themselves exhibited an important scattering, ranging from +12.6% to -20%, compared to their mean value, mainly due to differences in the weight of each carriage and the interaction with the induced inverse bending. Moreover, this difference could be attributed to potential occurrence of maximum strain values at a point of time between two consecutive samplings. In that case, the recorder value would be slightly lower than the actual one.

- The decrease in strain recorder between consecutive axis is lower, compared to the numerical calculations. This depicts an “inertia” of the material behavior (i.e. delay in unloading) which was not taken into consideration during modeling (no dynamic effects were simulated).
- The slight compression loading, which is monitored when the train enters the bridge from the opposite side compared to the sensor’s position, are present in both the numerical and the experimental results. Slight differences in time and duration of compression occurrence are noticed, especially during the crossing of four consecutive axis.

The above mentioned differences are attributed to certain error factors, which are listed below together with an estimation of the magnitude of the induced error:

- *Train weight:* The train weight was not known accurately and was estimated to correspond to the train’s tare weight, plus 2/3 and 3/3 of the maximum payload. (Important error)
- *Bridge angle:* As it was mentioned earlier, one track was 0.121m higher compared to the other, which leads to non-uniform load distribution between the wheels of the axis. (Small error)
- *Dynamic effects:* The train speed in combination with the bridge angle is causing dynamic effects, which were not taken into consideration in the numerical model. This led to both qualitative (e.g. strain “unloading” between two consecutive axis loading) and quantitative (maximum strain values) deviations. It should be noted that from similar studies, a dynamic magnification factor in the area of 15% would be expected, which fully explains the differences observed between the maximum calculated compared to the maximum measured values (Important error).
- *Adhesive layer:* The adhesive layer used for sensor bonding is functioning like a strain absorber, during strain transfer from the beam to the sensor (Small error).
- *Materials:* Given that the exact manufacturing material was now known, the mild steel properties were used for the numerical simulation. Moreover, a linearly elastic behavior of the material was assumed, which may not be true for certain areas, due to ageing and extensive usage of the bridge: existence of local plasticity areas which may differentiate overall bridge behavior. (Small error)
- *Expansion gaps:* The experimentally measured strain versus time diagram includes abrupt strain variations, which are attributed to the existence of expansion gaps in the vicinity of the sensor. Such effect was not numerically modeled. However, as this effect does not take place simultaneously with the maximum measured strain, it’s effect is not important.

6. Conclusions

According to the results listed above, it was concluded that, despite the existence of numerous error factors, initial results concerning the application of the structural health monitoring methodology on steel railway bridge could be retrieved, by using optical fiber sensors and the finite element method. Both the sensitivity (1 μ m) and the sampling frequency (100Hz) could be considered as adequate, for this specific case. However, it would be recommended to perform the same study using higher sampling frequency, in order to evaluate potential effect on maximum recorded values. It is well understood that these monitoring results would only concern the beam under which the sensor was bonded. Additional sensors should be installed in order to monitor the whole bridge, preferably under every beam section. Moreover, the performance of equivalent studies including representative artificial failures should be performed, in order to evaluate the range of the failure effect and its detectability by the sensor, as well as to compare measured strains with finite element models simulating the structure with the failures.

7. Acknowledgements

The authors gratefully acknowledge the assistance provided by the Smart Fibers Ltd, through the provision of both scientific - technical data and the availability of hardware.

8. References

- [1] W. Stawenski et al, Health Monitoring of Aerospace structures, Wiley, 2004.
- [2] Proceedings of the 1st European Conference on Structural Health Monitoring 2002, Edited by Daniel L. Balageas, Destech Publications, ENS Cachan France, July 10-12, 2002.
- [3] Proceedings of the 2nd European Conference on Structural Health Monitoring 2004, Edited by Christian Boller Wieslaw Staszewski, Destech Publications, Forum am Deutschen Museum, Munich, Germany, July 7-9 2004.
- [4] G.J. Tsamasphyros, N. K. Furnarakis, G.N. Kanderakis, Z.P. Marioli-Riga, “Three-Dimensional Finite Element Analysis of Composite Patches with Embedded Optical Fibres – Through Thickness Optimization”, ICCES 01, Puerto Vallarta, Mexico, 19-24 August 2001.
- [5] G. J. Tsamasphyros, G. N. Kanderakis, N. K. Furnarakis, Z. P. Marioli-Riga, R. Chemama, R. Bartolo, Three – Dimensional Finite Element Analysis of composite patches with embedded optical fibers – Selection of Optical Fibers Paths and Sensors Locations, Structural Health Monitoring 2002, Daniel L. Balageas, 1203-1210, Destech Publications, ENS Cachan France, July 10-12, 2002.
- [6] G. J. Tsamasphyros, N. K. Furnarakis, G. N. Kanderakis, Z. P. Marioli-Riga, Three – Dimensional Finite Element Analysis of composite patches with embedded optical fibers – Optimizing Optical Fiber Embedding Location: Structural Health Monitoring 2002, Daniel L. Balageas, 1219-1226, Destech Publications, ENS Cachan France, July 10-12, 2002.
- [7] G. Tsamasphyros, G. N. Kanderakis, N.K. Furnarakis, Z. P. Marioli-Riga, Optimization of Embedded Optical Sensor Locations in Composite Repairs Applied Composite Materials Volume 10 No3: 129-140, May 2003, Kluwer Academic Publishers, Netherlands.
- [8] G. J. Tsamasphyros, G. N. Kanderakis, N. K. Fournarakis, Z. P. Marioli-Riga, Detection of patch debonding in composite repaired cracked metallic specimens, using optical fibers and sensors SPIE Optical Metrology Conference, 23-26 June 2003, Munich, Germany.
- [9] S. Crossley, Z. Marioli-Riga, G. Tsamasphyros, G. Kanderakis, N. Furnarakis, A. Ikiades, M. Konstantaki, “Smart Patches : Self-monitoring composite patches for the repair of aircraft”, SPIE’s Proc, Int. Symp. on Opt. Tech. for Industrial and Environmental Sensing, Conf. on Intel. Transp. Sensors and Controls, Vol 5272B, Providence, RI, USA, Oct 29-Nov 3 2003.
- [10] Eric Udd, Fiber Optic Smart Structures, Wiley-Interscience Publications, 1995
- [11] J. Sirkis et al. “What do embedded optical fibers really measures?”, SPIE, Vol.1777, 1992,N. Spon Ltd, 1981, London & NY.
- [12] Smart Patch[®] - W3/2100 Specifications, www.smartfibres.com
- [13] Optical Interrogator Specifications, www.micronoptics.com
- [14] SP 106 Specifications, www.spsystems.com
- [15] G. Tsamasphyros, E.E. Theotokoglou, The Finite Element Method, Athens 1994, Chapter 3.4.